Astronomy & Astrophysics manuscript no. ms3386 February 2, 2008
(DOI: will be inserted by hand later)

arXiv:astro-ph/0309138v1 4 Sep 2003

Sulphur chemistry in the envelopes of massive young stars

F.F.S. van der Tak[1], A.M.S. Boonman[2], R. Braakman[2], and E.F. van Dishoeck[2]

[1] Max-Planck-Institut für Radioastronomie, Auf dem Hügel 69, 53121 Bonn, Germany
[2] Sterrewacht, Postbus 9513, 2300 RA Leiden, The Netherlands

Received 6 December 2002 / Accepted 4 September 2003

Abstract. The sulphur chemistry in nine regions in the earliest stages of high-mass star formation is studied through single-dish submillimeter spectroscopy. The line profiles indicate that 10–50% of the SO and SO_2 emission arises in high-velocity gas, either infalling or outflowing. For the low-velocity gas, excitation temperatures are 25 K for H_2S, 50 K for SO, H_2CS, NS and HCS^+, and 100 K for OCS and SO_2, indicating that most observed emission traces the outer parts ($T < 100$ K) of the molecular envelopes, except high-excitation OCS and SO_2 lines. Abundances in the outer envelopes, calculated with a Monte Carlo program, using the physical structures of the sources derived from previous submillimeter continuum and CS line data, are $\sim 10^{-8}$ for OCS, $\sim 10^{-9}$ for H_2S, H_2CS, SO and SO_2, and $\sim 10^{-10}$ for HCS^+ and NS. In the inner envelopes ($T > 100$ K) of six sources, the SO_2 abundance is enhanced by a factor of ∼100–1000. This region of hot, abundant SO_2 has been seen before in infrared absorption, and must be small, $\lesssim 0''.2$ (180 AU radius). The derived abundance profiles are consistent with models of envelope chemistry which invoke ice evaporation at $T \sim 100$ K. A major sulphur carrier in the ices is probably OCS, not H_2S as most models assume. Shock chemistry is unlikely to contribute.The source-to-source abundance variations of most molecules by factors of ∼10 do not correlate with previous systematic tracers of envelope heating. Without observations of H_2S and SO lines probing warm ($\gtrsim 100$ K) gas, sulphur-bearing molecules cannot be used as evolutionary tracers during star formation.

Key words. ISM: molecules – Molecular processes – Stars: Circumstellar matter; Stars: formation

1. Introduction

Spectral line surveys at submillimeter wavelengths have revealed considerable chemical differences between star-forming regions (e.g., Blake et al. 1987; Sutton et al. 1995; Schilke et al. 1997; Helmich & van Dishoeck 1997; Hatchell et al. 1998a; Nummelin et al. 2000; see van Dishoeck 2001 for a complete list). While these differences indicate activity, the dependence of molecular abundances on evolutionary state and physical parameters is poorly understood. Better insight into this relation would be valuable for probing the earliest, deeply embedded phases of star formation where diagnostics at optical and near-infrared wavelengths are unavailable. This is especially true for the formation of high-mass stars, for which the order in which phenomena occur is much less well understood than in the low-mass case, and for which the embedded phase is a significant fraction (≈10%) of the total lifetime of $\sim 10^6$ yr.

Sulphur-bearing molecules are attractive as candidate tracers of early protostellar evolution (Hatchell et al. 1998b; Buckle & Fuller 2003). In models of "hot cores" (Charnley 1997), where the chemistry is driven by the evaporation of icy grain mantles due to protostellar heating, the abundances of sulphur-bearing molecules exhibit a characteristic variation with time. After its release from the grain mantles, H_2S is converted into SO and SO_2 in $\sim 10^3$ yr, and further into CS, H_2CS and OCS after $\sim 10^5$ yr. This type of model has had some success in reproducing the chemistry of star-forming regions (Langer et al. 2000).

Besides thermal heating, shocks are potentially relevant to the chemistry in star-forming regions. Young stars drive outflows which expose their surroundings to the effects of shocks. The submillimeter lines of SO_2 in Orion are very broad, and likely arise in the outflow (Schilke et al. 1997). Models of chemistry behind interstellar shocks (Mitchell 1984; Leen & Graff 1988; Pineau des Forêts et al. 1993) predict enhancements of H_2S, SO and SO_2 on time scales of $\sim 10^4$ yr. Thus, both by ice evaporation and by shock interaction, sulphur could act as a clock on the time scale of 10^4 yr relevant for the embedded phase of star formation.

This paper uses submillimeter observations of sulphur-bearing molecules to test models of chemistry during star formation, and attempts to order these regions chronologically. The sources are nine regions of high-mass star for-

---

Send offprint requests to: vdtak@mpifr-bonn.mpg.de

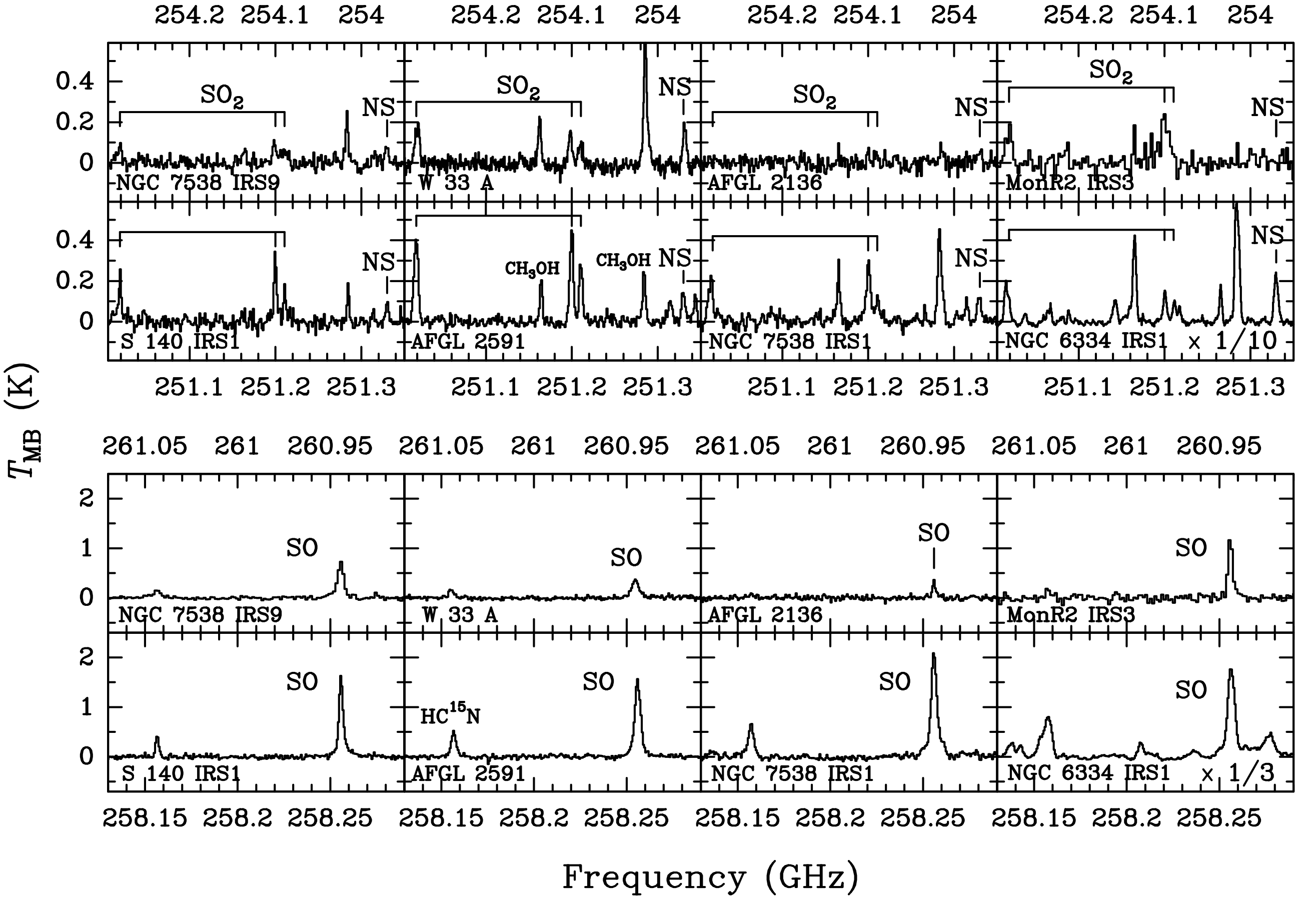

Fig. 1. Two examples of spectral settings toward eight of our sources, showing differences in the relative and in the absolute strengths of lines of sulphur-bearing molecules. The top and bottom frequency scales are the two receiver sidebands. The data for NGC 6334 IRS1 have been divided by 10 and 3 respectively, for clarity. The non-labeled lines are due to non-sulphur-bearing molecules, of which the strongest are labeled in the AFGL 2591 panels.

mation with luminosities $1 \times 10^4 - 2 \times 10^5$ L$_\odot$ at distances of $1 - 4$ kpc (Table 1). Originally selected for their mid-infrared brightness, the sources were found to have large envelope masses (40-1100 M$_\odot$ within $r = 0.15 - 0.36$ pc) based on submillimeter data (van der Tak et al. 2000b). Together with their weak radio emission and their strong molecular outflows, these masses indicate very early evolutionary stages, probably preceding the formation of hot cores. Two of our sources may be more evolved than the others: NGC 6334 IRS1, which has a very rich, 'hot core'-type submillimeter spectrum (McCutcheon et al. 2000; Thorwirth et al., in prep.), and NGC 7538 IRS1, which has strong free-free emission.

Observations of CH_3OH lines towards some of these sources (van der Tak et al. 2000a) indicate an increase in the CH_3OH abundance by a factor of 100 in the warm inner envelope, which is likely due to evaporation of CH_3OH-rich ices. The excitation of CH_3OH, as well as that of CO and C_2H_2, correlates well with other temperature tracers, such as the gas/solid ratios of CO_2 and H_2O, the 45/100 μm colour and the fraction of heated solid $^{13}CO_2$ (Boogert et al. 2000; van der Tak et al. 2000b; Boonman et al. 2003). Since these quantities also correlate with the ratio of envelope mass to stellar mass, their variation likely reflects evolution through the dispersal of the protostellar envelopes. These findings make the sample a good testbed for theories of chemical evolution during the earliest deeply embedded phases of high-mass star formation.

2. Observations

The data presented in this paper are part of a targeted spectral line survey of embedded massive stars, aimed to track chemical evolution during the earliest stages of high-mass star formation. Fifteen frequency settings have been observed, which also contain many lines of sulphurless molecules. Some of these data have been published by van der Tak et al. (1999, 2000a,b). These observations were performed with the 15-m James Clerk

Maxwell Telescope (JCMT)[1] on Mauna Kea, Hawaii between 1995 and 1998. The beam size (FWHM) and main beam efficiency of the antenna were 18″ and 64 − 69% at 230 GHz and 14″ and 58 − 63% at 345 GHz. The frontends were the receivers A2, B3 and B3i; the backend was the Digital Autocorrelation Spectrometer, covering 500 MHz instantaneous bandwidth. Pointing was checked every 2 hours during the observing and was always found to be within 5″. To subtract the atmospheric and instrumental background, the chopping secondary was used with 180″ offsets. Total integration times are 30–40 minutes for each frequency setting. Figure 1 shows examples of the data towards all but one of our sources; the data on W3 IRS5 were presented by Helmich & van Dishoeck (1997).

Additional observations of H_2S and OCS in the 130-180 GHz window were carried out with the 30-m telescope of the Institut de Radio Astronomie Millimétrique (IRAM)[2] on Pico Veleta, Spain, in August 2002. The frontend was the facility receiver C150 and the backend the Versatile Spectral Assembly (VESPA) autocorrelator. Integration times were 10-20 minutes using frequency switching with a throw of 7.3 MHz. Data were calibrated onto $T_{\rm MB}$ scale by multiplying by 1.43, the ratio of forward and main beam efficiencies. The beam size is 15″ at these frequencies.

The H_2S 393 GHz line was observed in May 1995 at the 10.4-m Caltech Submillimeter Observatory (CSO)[3], with the facility receiver as frontend and the 50 MHz AOS as backend. The telescope has a beam size of 25″ and a main beam efficiency of 60% at this frequency.

Reduction was carried out using the CLASS package developed at IRAM. Linear baselines were subtracted and the spectra were smoothed once and calibrated onto $T_{\rm MB}$ scale. Only the frequency switched 30m data required higher order polynomials to fit the baseline. The final spectra have a resolution of $0.3 - 1.5$ km s^{-1} and rms noise levels (in $T_{\rm MB}$) of $20 - 30$ mK for the 150 and 230 GHz bands, and $30 - 50$ mK for the 345 GHz band. Multiplying these values by the line width (Table 4) yields the uncertainties of the line fluxes in Table 3. Although the absolute calibration is only correct to ≈30%, the relative strength of lines within one frequency setting is much more accurate.

Line identification was performed using the JPL catalog (Pickett et al. 1998)[4]. A matching frequency is the main criterion for assignment, but the upper energy level of the transition and the complexity of the molecule are

Table 2. Observed transitions

Molecule	Transition	Frequency (MHz)	$E_{\rm up}$ (K)	Telescope
H_2CS	$J_{K_pK_o} = 7_{16} \rightarrow 6_{15}$	244047.8	60.0	JCMT
H_2CS	$J_{K_pK_o} = 10_{19} \rightarrow 9_{18}$	348531.9	105.2	JCMT
HCS^+	$J = 6 \rightarrow 5$	256027.8	43.0	JCMT
HCS^+	$J = 8 \rightarrow 7$	341350.8	73.7	JCMT
H_2S	$J_{K_pK_o} = 1_{10} \rightarrow 1_{01}$	168762.8	27.9	IRAM
H_2S	$J_{K_pK_o} = 2_{11} \rightarrow 2_{02}$	393450.5	73.6	CSO
H_2S	$J_{K_pK_o} = 2_{20} \rightarrow 2_{11}$	216710.4	84.0	JCMT
NS	$^2\Pi_{1/2}\ J = 11/2 \rightarrow 9/2$	253969 [a]	39.9	JCMT
NS	$^2\Pi_{1/2}\ J = 15/2 \rightarrow 13/2$	346220 [b]	71.0	JCMT
OCS	$J = 13 \rightarrow 12$	158107.4	53.1	IRAM
OCS	$J = 28 \rightarrow 27$	340449.2	237.0	JCMT
OCS	$J = 30 \rightarrow 29$	364749.0	271.4	JCMT
$OC^{34}S$	$J = 18 \rightarrow 17$	213553.1	97.4	JCMT
$OC^{34}S$	$J = 22 \rightarrow 21$	260991.8	144.1	JCMT
SO	$N_J = 5_6 \rightarrow 4_5$	219949.4	35.0	JCMT
SO	$N_J = 6_6 \rightarrow 5_5$	258255.8	56.5	JCMT
SO	$N_J = 6_7 \rightarrow 5_6$	261843.7	47.6	JCMT
SO	$N_J = 8_7 \rightarrow 7_6$	340714.2	81.2	JCMT
SO	$N_J = 8_8 \rightarrow 7_7$	344310.6	87.5	JCMT
SO	$N_J = 8_9 \rightarrow 7_8$	346528.5	78.8	JCMT
^{34}SO	$N_J = 8_8 \rightarrow 7_7$	337582.2	86.1	JCMT
SO_2	$J_{K_pK_o} = 5_{24} \rightarrow 4_{13}$	241615.8	23.6	JCMT
SO_2	$J_{K_pK_o} = 5_{33} \rightarrow 4_{22}$	351257.2	35.9	JCMT
SO_2	$J_{K_pK_o} = 5_{33} \rightarrow 5_{24}$	256246.9	35.9	JCMT
SO_2	$J_{K_pK_o} = 5_{51} \rightarrow 6_{42}$	345149.0	75.1	JCMT
SO_2	$J_{K_pK_o} = 6_{33} \rightarrow 6_{24}$	254280.5	41.4	JCMT
SO_2	$J_{K_pK_o} = 7_{35} \rightarrow 7_{26}$	257100.0	47.8	JCMT
SO_2	$J_{K_pK_o} = 8_{35} \rightarrow 8_{26}$	251210.6	55.2	JCMT
SO_2	$J_{K_pK_o} = 9_{37} \rightarrow 9_{28}$	258942.2	63.5	JCMT
SO_2	$J_{K_pK_o} = 10_{64} \rightarrow 11_{57}$	350862.7	138.8	JCMT
SO_2	$J_{K_pK_o} = 11_{1,11} \rightarrow 10_{0,10}$	221965.2	60.4	JCMT
SO_2	$J_{K_pK_o} = 11_{39} \rightarrow 11_{2,10}$	262256.9	82.8	JCMT
SO_2	$J_{K_pK_o} = 13_{1,13} \rightarrow 12_{0,12}$	251199.7	82.2	JCMT
SO_2	$J_{K_pK_o} = 14_{0,14} \rightarrow 13_{1,13}$	244254.2	93.9	JCMT
SO_2	$J_{K_pK_o} = 15_{6,10} \rightarrow 16_{5,11}$	253956.6	198.6	JCMT
SO_2	$J_{K_pK_o} = 16_{4,12} \rightarrow 16_{3,13}$	346523.9	164.5	JCMT
SO_2	$J_{K_pK_o} = 18_{1,17} \rightarrow 18_{0,18}$	240942.8	163.1	JCMT
SO_2	$J_{K_pK_o} = 18_{4,14} \rightarrow 18_{3,15}$	338306.0	196.8	JCMT
SO_2	$J_{K_pK_o} = 19_{1,19} \rightarrow 18_{0,18}$	346652.2	168.1	JCMT
SO_2	$J_{K_pK_o} = 20_{1,19} \rightarrow 19_{2,18}$	338611.8	198.9	JCMT
SO_2	$J_{K_pK_o} = 22_{2,20} \rightarrow 22_{1,21}$	216643.3	248.4	JCMT
SO_2	$J_{K_pK_o} = 24_{2,22} \rightarrow 23_{3,21}$	348387.8	292.7	JCMT
SO_2	$J_{K_pK_o} = 25_{3,23} \rightarrow 25_{2,24}$	359151.2	320.9	JCMT
SO_2	$J_{K_pK_o} = 28_{2,26} \rightarrow 28_{1,27}$	340316.4	391.8	JCMT
$^{34}SO_2$	$J_{K_pK_o} = 7_{44} \rightarrow 7_{35}$	345519.7	63.6	JCMT
$^{34}SO_2$	$J_{K_pK_o} = 10_{46} \rightarrow 10_{37}$	344245.4	88.4	JCMT
$^{34}SO_2$	$J_{K_pK_o} = 11_{39} \rightarrow 11_{2,10}$	253936.3	81.9	JCMT
$^{34}SO_2$	$J_{K_pK_o} = 15_{2,14} \rightarrow 14_{1,13}$	358988.0	118.7	JCMT
$^{34}SO_2$	$J_{K_pK_o} = 19_{1,19} \rightarrow 18_{0,18}$	344581.1	167.4	JCMT
$^{34}SO_2$	$J_{K_pK_o} = 29_{9,21} \rightarrow 30_{8,22}$	257466.7	590.7	JCMT

[a] Blend of the $F = 7 \rightarrow 6$, $F = 6 \rightarrow 5$ and $F = 5 \rightarrow 4$ hyperfine components

[b] Blend of the $F = 9 \rightarrow 8$, $F = 8 \rightarrow 7$ and $F = 7 \rightarrow 6$ hyperfine components

---

[1] The James Clerk Maxwell Telescope is operated by the Joint Astronomy Centre, on behalf of the Particle Physics and Astronomy Research Council of the United Kingdom, the Netherlands Organization for Scientific Research and the National Research Council of Canada.

[2] IRAM is an international institute for research in millimeter astronomy, cofunded by the Centre National de la Recherche Scientifique (France), the Max Planck Gesellschaft (Germany), and the Instituto Geografico Nacional (Spain).

[3] The CSO is supported by NSF grant AST 99-80846.

[4] http://spec.jpl.nasa.gov

Table 1. Source sample.[a]

Source	R.A. (1950) (h m s)	Dec. (1950) (° ′ ″)	L (10^4 L$_\odot$)	d (kpc)	N(H$_2$) (10^{23} cm^{-2})
W3 IRS5	02 21 53.1	+61 52 20	17	2.2	2.3
MonR2 IRS3	06 05 21.5	–06 22 26	1.3	0.95	1.8
NGC 6334 IRS1	17 17 32.0	–35 44 05	11	1.7	11.3
W33A	18 11 43.7	–17 53 02	10	4	6.2
AFGL 2136	18 19 36.6	–13 31 40	7	2	1.2
AFGL 2591	20 27 35.8	+40 01 14	2	1	2.3
S140 IRS1	22 17 41.1	+63 03 42	2	0.9	1.4
NGC 7538 IRS1	23 11 36.7	+61 11 51	13	2.8	6.5
NGC 7538 IRS9	23 11 52.8	+61 10 59	4	2.8	3.3

[a] Luminosity and distance from Henning et al. (1992) and Giannakopoulou et al. (1997) (MonR2 IRS3) and from van der Tak et al. (2000b) (other sources); H_2 column density from this work (MonR2 IRS3) and from van der Tak et al. (2000b) (other sources).

also considered. Table 2 has details about the observed transitions.

For each detected feature, a satisfying match could be found in the catalog within 0.5 MHz, except for the H_2CS $10_{19} - 9_{18}$ line at 348.5 GHz, whose residual is 2 MHz. Laboratory spectroscopy of H_2CS only exists up to 250 GHz (Beers et al. 1972), and the analysis in the JPL catalog only includes pure rotation and centrifugal distortion terms. At higher frequencies and for higher J-values, higher order terms become important, which may be why the catalog prediction is inaccurate for this line. Our data indicate a frequency of 348534.2 MHz.

3. Results

3.1. Line profiles

We have fitted the detected lines with Gaussian profiles. Table 3 reports the observed fluxes and Table 4 the widths of the lines. While most lines could be satisfactorily fitted with a single Gaussian, the lines of SO, which are the strongest lines that we have observed, required two Gaussians for a good fit to their profiles (Fig. 2; Table 4). One component agrees in position and width with the values measured for $C^{17}O$ and $C^{34}S$ by van der Tak et al. (2000b) and is attributed to a static envelope. Table 5 reports similar measurements for the source MonR2 IRS3 which van der Tak et al. did not study. The other component has 2.8 times as large a width on average. This high-velocity emission may trace outflowing or infalling motions. The contributions from high- and low-velocity gas to the SO line fluxes are about equal, unlike CS, where the envelope carries 90% of the fluxes (van der Tak et al. 2000b; Table 5). The infrared absorption and submillimeter emission lines of CO towards these sources also show multiple velocity components (Mitchell et al. 1991; Mitchell & Hasegawa 1991; Mitchell et al. 1992). However, the velocities do not match in detail, as expected because of differences in spectral and angular resolution between infrared and submillimeter data on one hand, and excitation differences between CO and SO on the other.

The fit of two Gaussians to the SO lines is excellent, which is not always the case for CO. An alternative method is to use area integrals, which do not attribute any low-velocity gas to the high-velocity component. Our approach may overestimate the high-velocity contribution to the line flux by factors up to 2.

The ratios of the high- to low-velocity contributions to the SO lines are $\lesssim 1$ for the lines in the 230 GHz band, and $\gtrsim 1$ for the lines in the 345 GHz band. This difference could be due to the higher temperatures and densities required for excitation of the 345 GHz lines, or to the smaller beams in which they are observed. Since the high-velocity wings on the CS lines in these sources also become more pronounced in smaller beams, independent of transition (van der Tak et al. 2000b), the broad component probably is more compact than the envelope, but not necessarily warmer or denser. The high-velocity gas in these sources thus seems to be confined to small radii. This situation differs from that in molecular clouds, where line width increases with size, and from that in many molecular outflows, where velocities usually increase with radius (e.g., Lee et al. 2002). However, while CO data show arcminute-sized outflows in our sources, higher velocities naturally occur at smaller radii in the case of infall. For example, gas at 1,000 AU (1″ at 1 kpc) in free fall onto a 10 M$_\odot$ object would have $V_{\rm inf} = 4$ km s^{-1}, consistent with the observed width of the broad component (Table 4).

The broad component peaks at slightly more blueshifted velocities (by 0.17 km s^{-1} on average) than the envelope, a situation found before for CS and H_2CO (van der Tak et al. 2000b). In the case of outflow, obscuration by $A_V = 10^4$ mag of dust could explain the absence of redshifted wings. Since some redshifted SO is seen (Fig. 2), the requirement relaxes to several 1000 mag. Of the sources discussed here, only NGC 6334 IRS1 may have such a large amount of dust in its envelope (Table 1); the other sources may need circumstellar disks seen face-on. In the case of infall, a mixture of absorption and emission is

Table 3. Observed line fluxes $\int T_{\rm MB} dV$ (K km s^{-1}) from Gaussian fits, and 1σ upper limits. Dots denote missing data.

Transition	W3[a]	AFGL	NGC 7538		MonR2	S140	NGC6334	AFGL	W33A
	IRS5	2591	IRS1	IRS9	IRS3	IRS1	IRS1	2136	
$H_2CS\ 7_{16} \rightarrow 6_{15}$	0.8	1.4	3.8	1.6	0.9	1.5	10.6	0.3	2.9
$H_2CS\ 10_{19} \rightarrow 9_{18}$	<0.3	1.1	3.5	1.2	0.3	0.8	...	1.0	3.6
$HCS^+\ 6 \rightarrow 5$	0.3	...	...	...	...	...	...	...	...
$HCS^+\ 8 \rightarrow 7$	0.3	0.6	1.6	0.8	...	0.7	16.6	0.3	1.1
$H_2S\ 1_{10} \rightarrow 1_{01}$	9.4	13.1	15.4	7.7	7.6	14.3	...	6.7	17.8
$H_2S\ 2_{11} \rightarrow 2_{02}$	2.6	...	1.6	...	...	...	...	...	...
$H_2S\ 2_{20} \rightarrow 2_{11}$	2.2	0.8	1.9	0.4	<0.2	0.6	22.8	<0.1	1.9
NS $11/2 \rightarrow 9/2$	...	0.9	0.9	0.5	<0.4	0.5	15.9	<0.2	2.2
NS $15/2 \rightarrow 13/2$	...	<0.8	<1.2	...	...	...	11.6	...	2.8
OCS $13 \rightarrow 12$	...	0.4	0.8	0.3	...	<0.3	...	...	...
OCS $28 \rightarrow 27$	0.9	0.3	...	...	...	...	...	...	2.6
OCS $30 \rightarrow 29$	<0.4	0.3	...	...	...	...	...	...	...
$OC^{34}S\ 18 \rightarrow 17$	...	...	...	...	...	...	4.8	...	0.4
$OC^{34}S\ 22 \rightarrow 21$	<0.1	...	...	...	...	...	11.6	...	...
SO $5_6 \rightarrow 4_5$	17.4	9.9	8.4	1.3	3.7	10.8	...	2.0	3.0
broad	11.2	4.5	6.5	5.2	3.6	3.7	...	1.2	5.1
SO $6_6 \rightarrow 5_5$	26.1	5.3	5.8	2.5	3.5	4.0	26.1[c]	0.4	3.1[c]
broad	22.1	2.5	5.7	1.5	1.4	2.6	...	0.6	...
SO $6_7 \rightarrow 5_6$	14.7	7.3	10.0	3.0	4.8	5.7	...	1.5	3.5
broad	13.2	3.7	7.3	3.0	3.1	4.7	...	1.3	5.6
SO $8_7 \rightarrow 7_6$	17.9	3.7	6.5[b]	1.3	...	2.6	14.5	<0.2	1.8[c]
broad	26.8	5.1	...	2.4	...	5.5	23.4	<0.2	...
SO $8_8 \rightarrow 7_7$	31.7	3.4	9.5	4.7[b]	...	2.6	47.3[c]	1.5	4.1
broad	28.8	4.5	6.7	..	...	5.0	...	0.5	6.4
SO $8_9 \rightarrow 7_8$	27.9	5.6	8.3	1.5	3.6	3.9	26.4	1.4[c]	2.2
broad	58.1	5.1	5.9	3.9	5.7	6.0	34.4	...	6.7
$^{34}SO\ 8_8 \rightarrow 7_7$	18.9	2.7	0.9	<0.3	...	<0.4	19.6	...	<0.7
$SO_2\ 5_{24} \rightarrow 4_{13}$	8.2	2.3	2.0	0.7	1.0	1.1	6.8[d]	...	...
$SO_2\ 5_{33} \rightarrow 4_{22}$	12.2	...	...	...	...	...	...	...	2.9
$SO_2\ 5_{33} \rightarrow 5_{24}$	6.9	...	...	...	...	<1	...	...	...
$SO_2\ 5_{51} \rightarrow 6_{42}$	<0.3	...	...	...	...	...	7.1	...	...
$SO_2\ 6_{33} \rightarrow 6_{24}$	20.8	3.0	1.7	0.6	1.6	1.1	12.1	<0.1	2.2
$SO_2\ 7_{35} \rightarrow 7_{26}$	10.2	1.7	1.1	<0.4	0.7	0.5	...	...	1.0
$SO_2\ 8_{35} \rightarrow 8_{26}$	12.7	1.7	0.9	0.4	0.7	0.7	5.9	<0.2	1.4
$SO_2\ 9_{37} \rightarrow 9_{28}$	9.6	2.4	1.5	<0.2	...	<0.5	...	...	3.7
$SO_2\ 10_{64} \rightarrow 11_{57}$	3.4	1.7	<0.4	...	...	...	...	...	0.8
$SO_2\ 11_{1,11} \rightarrow 10_{0,10}$	...	...	...	...	...	...	...	0.3	...
$SO_2\ 11_{39} \rightarrow 11_{2,10}$	...	...	...	...	...	...	...	...	1.6
$SO_2\ 13_{1,13} \rightarrow 12_{0,12}$	19.0	2.7	2.2	0.7	1.5	1.5	8.8	<0.2	1.7
$SO_2\ 14_{0,14} \rightarrow 13_{1,13}$	12.2	2.8	1.7	...	1.3	1.3	...	0.3	1.9
$SO_2\ 15_{6,10} \rightarrow 16_{5,11}$	...	0.6	...	...	...	...	...	...	...
$SO_2\ 16_{4,12} \rightarrow 16_{3,13}$	29.5	...	...	...	...	...	...	0.6	2.0
$SO_2\ 18_{1,17} \rightarrow 18_{0,18}$	7.7	1.0	...	...	...	...	...	...	0.7
$SO_2\ 18_{4,14} \rightarrow 18_{3,15}$	13.3	2.9	...	...	1.2	...	...	...	1.3
$SO_2\ 19_{1,19} \rightarrow 18_{0,18}$	31.7	2.6	<0.4	<0.4	...	<0.7	7.0	0.4	...
$SO_2\ 20_{1,19} \rightarrow 19_{2,18}$	16.0	2.7	...	...	...	...	...	...	...
$SO_2\ 22_{2,20} \rightarrow 22_{1,21}$	5.5	0.8	...	...	...	...	1.7	...	0.5
$SO_2\ 24_{2,22} \rightarrow 23_{3,21}$	6.1	3.2	<0.6	...	...	...	...	...	...
$SO_2\ 25_{3,23} \rightarrow 25_{2,24}$	4.1	2.8	1.4	...	...	...	...	...	1.0
$SO_2\ 28_{2,26} \rightarrow 28_{1,27}$	11.3	...	...	...	...	...	...	...	0.6
$^{34}SO_2\ 7_{44} \rightarrow 7_{35}$	2.4	1.0	...	...	...	...	...	...	...
$^{34}SO_2\ 10_{46} \rightarrow 10_{37}$	2.5	1.1	...	...	...	...	...	...	...
$^{34}SO_2\ 11_{39} \rightarrow 11_{2,10}$	...	1.1	...	...	...	...	...	...	0.8
$^{34}SO_2\ 15_{2,14} \rightarrow 14_{1,13}$	0.7	1.1	...	...	...	...	...	...	0.8
$^{34}SO_2\ 19_{1,19} \rightarrow 18_{0,18}$	5.8	1.2	<0.4	<0.4	...	<0.4	...	...	...
$^{34}SO_2\ 29_{9,21} \rightarrow 30_{8,22}$	<0.2	...	...	...	...	...	...	...	0.3

[a] From Helmich & van Dishoeck (1997), except SO

[b] Attributed to envelope based on center velocity

[c] Attributed to envelope based on line width

[d] Difficult fit due to partial blend with other lines

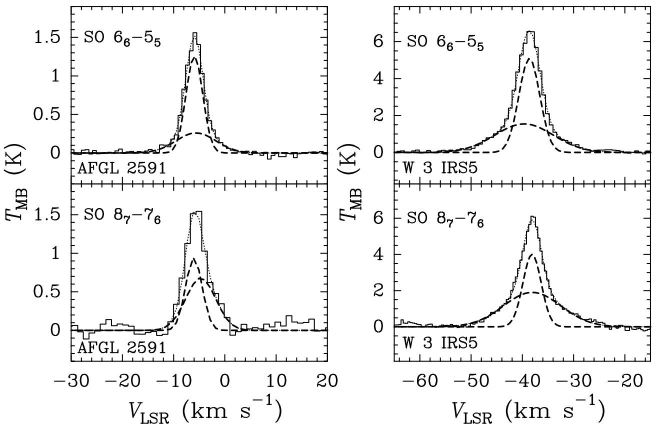

Fig. 2. Observed velocity profiles of the SO 6_6–5_5 and 8_7–7_6 lines in the sources AFGL 2591 and W3 IRS5, showing the low- and high-velocity components. The dashed lines are our fits to the individual components and the dotted line is the sum of the two components.

Table 5. Observations of CS, $C^{34}S$ and $C^{17}O$ lines towards MonR2 IRS3.

Line	Frequency (MHz)	T_{MB} (K)	ΔV (km s^{-1})	$\int T_{MB} dV$ (K km s^{-1})
CS $5 \rightarrow 4$	244935.6	9.2	2.7	27
	broad	0.2	8.0	1.9
CS $7 \rightarrow 6$	342883.0	6.6	2.5	17.8
	broad	0.3	8.0	2.4
CS $10 \rightarrow 9$	489751.0	2.0	2.7	5.6
$C^{34}S$ $5 \rightarrow 4$	241016.2	0.6	2.3	1.4
$C^{34}S$ $7 \rightarrow 6$	337396.7	0.4	2.6	1.1
$C^{17}O$ $3 \rightarrow 2$	337060.9	2.3	2.6	6.4

expected at redshifted velocities (Choi 2002), which may partly cancel each other if unresolved, to give the impression of predominantly blueshifted emission. We conclude that both infall and outflow are plausible explanations for the high-velocity gas, and recommend interferometric observations of SO to decide between these options.

For most sources in our sample, the width of the SO_2 lines is between the values for the low- and high-velocity components. The only source where the SO_2 lines are strong enough to fit two components is W3 IRS5, where the line profiles do not show wings. However, most of these data, taken from Helmich & van Dishoeck (1997), were observed with an AOS as backend, and have lower spectral resolution than our data. It seems therefore plausible that, like for SO, about half of the SO_2 emission arises in high-velocity gas.

For the other molecules, the signal to noise ratio is not high enough to disentangle multiple velocity components. This paper assumes that these lines originate in low-velocity gas, which given our results for SO may overestimate column densities and abundances (§§ 3.3, 4) by factors of up to 2.

3.2. Excitation temperatures

For SO and SO_2, the number of detected lines is large enough to construct rotation diagrams. This method, described in detail by Blake et al. (1987) and Helmich et al. (1994), assumes that the lines are optically thin and that the molecular excitation can be described by a single temperature, the rotation temperature. If radiative decay competes with collisional excitation, the rotation temperature lies below the kinetic temperature. If the lines are optically thick, the rotation diagram underestimates the column density and overestimates the excitation temperature. Another complication is that the lines are measured in beams of unequal size, so that somewhat different volumes of gas are probed. Despite these caveats, the rotation diagram provides a useful first estimate of excitation conditions and molecular column densities, and a stepping stone towards a more sophisticated analysis (§ 4).

Table 6. Rotation temperatures (K). Numbers in brackets denote uncertainties.

Source	SO		SO_2	CH_3OH^c
	Narrow	Broad		
W3 IRS5	>100	>100	154(14)^a	73(32)
W33A	54(18)	96(64)	124(12)	155(19)
AFGL 2136	59(24)	34(9)	>200	143(12)
AFGL 2591	31(6)	>100	185(28)^b	163(9)
S140 IRS1	26(4)	>100	56(16)	41(4)
NGC 7538 IRS1	65(27)	61(25)	47(12)	189(30)
NGC 7538 IRS9	48(17)	45(15)	...	29(2)
MonR2 IRS3	47(20)	>100	125(35)	110(20)
NGC 6334 IRS1	75(72)	...	45(15)	213(37)

^{a} Better fit with two components: $T_{\rm rot}$= 70(14) & 254(20) K.
^{b} Better fit with two components: $T_{\rm rot}$= 47(11) & 197(67) K.
^{c} From JCMT data (van der Tak et al. 2000a; Boonman et al. 1999).

Table 6 presents the results. In the case of SO, separate fits were made to the low- and high-velocity components. For NGC 7538 IRS9, the detected SO_2 lines do not cover a large enough range of energy levels to constrain $T_{\rm rot}$. The derived temperatures are 30...70 K for SO and 50...190 K for SO_2, reflecting the available range of energy levels. Lower limits to $T_{\rm rot}$ are poor fits to the data, probably caused by optically thick lines. Indeed, the SO/^{34}SO and SO_2/$^{34}SO_2$ line ratios of 1.3...$\gtrsim$10 are below the isotopic abundance ratio of $^{32}S/^{34}S$=22, which indicates optical depths of a few in the SO and SO_2 lines.

Table 4. Widths ΔV (km s^{-1}) of the emission line components, averaged over transition. Numbers in brackets denote uncertainties in units of the last decimal, except when only one transition was observed. Dots denote missing data. For SO, values for the narrow and the broad components are reported, whose positions are also given.

Source	CS		SO (narrow)		SO (broad)		SO_2	OCS	H_2S	H_2CS	HCS^+
	V_{LSR}	ΔV	V_{LSR}	ΔV	V_{LSR}	ΔV					
W3 IRS5	−38.4(3)	2.7(11)	−38.7(5)	4.8(3)	−39.0(10)	13.5(14)	6.6(12)	3.5(20)	5.6(6)	2.9	1.1(4)
W33A	+37.5(9)	5.4(5)	+37.8(3)	3.6(2)	+36.9(10)	11.6(11)	5.0(3)	...	2.5	2.2(7)	...
AFGL 2136	+22.8(1)	3.1(4)	+22.9(2)	2.5(8)	+23.6(16)	6.5(13)	5.0(7)	4.1(2)[a]	5.4	6.0	5.4
AFGL 2591	−5.5(2)	3.3(6)	−6.0(3)	3.7(2)	−5.6(9)	8.6(15)	5.0(30)	4.50	4.1	5.1(12)	7.1
S140 IRS1	−7.0(2)	3.3(3)	−7.0(1)	2.5(2)	−8.1(2)	9.6(22)	1.9(10)	...	3.6	2.9(8)	1.0
NGC 7538 IRS1	−57.4(5)	4.1(14)	−57.5(4)	3.8(4)	−58.4(6)	11.5(39)	5.1(9)	3.8(1)	3.8(2)	3.2(4)	3.2
NGC 7538 IRS9	−57.2(3)	4.1(5)	−57.4(3)	3.2(8)	−55.9(5)	7.8(21)	3.5(8)	...	2.9(1)	2.9	2.6
MonR2 IRS3	+10.2(1)	2.4(2)	+10.1(1)	3.0(1)	+10.0(16)	8.2(4)	7.0(9)	3.1	4.0(5)	4.4	3.6
NGC 6334 IRS1	−7.4(2)	5.3(3)	−7.2(11)	4.1(1)	−7.4(13)	11.1(1)	5.2(10)	2.1	4.1(3)	3.5(1)	3.5

[a] Value for $OC^{34}S$

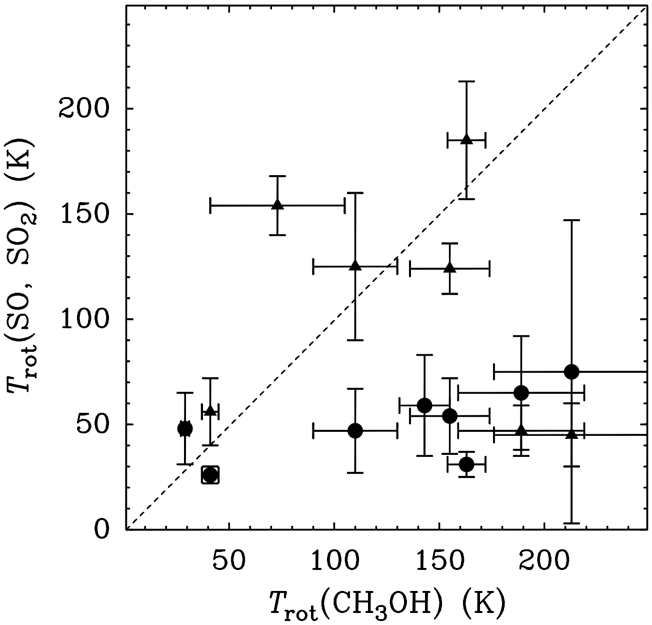

Fig. 3. Rotation temperatures of SO (dots) and SO_2 (triangles) versus values for CH_3OH.

The last column of Table 6 lists rotation temperatures of CH_3OH, measured previously. Strictly, these numbers are only lower limits to the kinetic temperatures in a 15″ beam, but they show good correlation with $T_{ex}(C_2H_2)$ which does directly trace the kinetic temperature (van der Tak et al. 2000a). The rotation temperatures of SO and SO_2 are not clearly correlated with T_{rot} (CH_3OH) within the uncertainties (Fig. 3). Therefore we cannot conclude at this point whether these molecules trace the same gas within the envelopes. In any case, differences in beam sizes and optical depth effects in the lines make it hard to draw firm conclusions before a more detailed radiative transfer analysis is presented in § 4.

For the other molecules, for which only few lines are available, the line ratios have been used to constrain T_{ex}. Source-averaged line ratios indicate $T_{ex}\approx50$ K for H_2CS, NS and HCS^+, $T_{ex}\approx25$ K for H_2S and $T_{ex}\approx100$ K for OCS. These values are only rough estimates, especially if based on few sources and/or lines.

3.3. Column densities

Table 7 presents beam-averaged molecular column densities, estimated from the observed line fluxes using the excitation temperatures found above. The column densities for H_2CS and H_2S are the sums of the ortho and para species, assuming an ortho to para ratio of 3. After calibration, the adopted T_{ex} is the main source of uncertainty in the column densities, especially if only one or two lines have been observed. For example, decreasing T_{ex} from 50 to 25 K increases column density estimates by factors of $\approx$2, while increasing T_{ex} from 50 to 75 K decreases column density estimates by $\lesssim 20\%$. In addition, column densities may have been underestimated by factors of a few due to nonnegligible optical depth.

To search for trends of column densities with temperature, Table 7 lists the sources in order of increasing $T(CH_3OH)$. The only trend seems to be that the warmest source has the largest column density of all molecules, except SO and SO_2. In order to investigate whether these trends in the column density reflect chemical differences between sources or are due to optical depth or beam size effects, a more detailed radiative transfer analysis is presented in § 4.

Table 7. Column densities (cm^{-2}) in 15–20″ beams.

Source	SO (10^{13})		SO_2	OCS	H_2S	H_2CS	NS	HCS^+
	Narrow	Broad	10^{13}	10^{13}	10^{13}	10^{12}	10^{12}	10^{11}
NGC 7538 IRS9	3	4	...	0.6	2	6	1	5
S140 IRS1	10	>6	7	<0.8	3	7	1	6
W3 IRS5	>27	>11	530^a	2	7	5	...	3
MonR2 IRS3	5	>5	15	...	3	4	<3	...
AFGL 2136	2	1	>3	...	2	4	<2	3
W33A	4	9	26	9	4	10	4	6
AFGL 2591	10	>7	52^b	1	3	6	2	5
NGC 7538 IRS1	12	9	11	2	5	15	2	11
NGC 6334 IRS1	40	...	46	24	60	30	20	84

[a] Better fit with two components: N=1.0 and 2.0 $\times 10^{15}$ cm^{-2}.
[b] Better fit with two components: N=1.6 and 5.5 $\times 10^{14}$ cm^{-2}.

3.4. Comparison with infrared data

Keane et al. (2001) observed the ν_3 band of SO_2 around 7.3 μm in absorption towards five of the sources studied here, and found column densities of SO_2 of a few 10^{16} cm^{-2}, a factor of $\sim$100 higher than the submillimeter data indicate. In contrast, infrared observations of CO and dust yield 3–5 times *lower* column densities than submillimeter data, as a result of non-spherical geometry on scales $\lesssim 1''$ (van der Tak et al. 2000b). Correcting for optical depth in the SO_2 submillimeter lines increases the column density estimate, but only by factors of a few (§ 3.2), which does not explain the discrepancy with the infrared values. More likely to be important are chemical effects on small scales. The sources are centrally concentrated, $n(H_2) \propto r^{-\alpha}$ with $\alpha = 1.0 - 1.5$, so that absorption data are more sensitive to warm, dense gas at small radii, while emission data probe more extended, cooler and less dense gas. The infrared excitation temperatures of 225–750 K also suggest that the SO_2 absorption arises in warm gas.

The infrared estimates of $N(SO_2)$ imply optically thick submillimeter lines of SO_2, but their brightness measured with the JCMT is much lower than the infrared T_{ex}. The implied limit on the source size is $\theta_S = 15''(T_{ex}/T_0)^{-0.5}$, with T_0 the typical T_{MB} of 0.1 K. Inferred values of θ_S range from 0.″17 for AFGL 2591 to 0.″32 for MonR2 IRS3, corresponding to linear radii of $100 - 250$ AU. The limited spectral resolution of the infrared data prohibits assignment of the absorbers to either velocity component in emission, which however does not affect our conclusion.

4. Radiative transfer analysis

4.1. Model description

To estimate molecular abundances we have used the Monte Carlo radiative transfer program by Hogerheijde & van der Tak (2000) [5]. Starting from radial profiles of the density and kinetic temperature, this program solves for the molecular excitation as a function of radius. Besides collisional excitation, radiation from the cosmic microwave background and thermal radiation from local dust are taken into account. The result is integrated over the line of sight and convolved with the appropriate telescope beam. Observed and synthetic line fluxes are compared with a χ^2 statistic to find the best-fit abundance. Initially, abundances were assumed to be constant with radius.

Molecular data were mostly taken from the database by Schöier et al. (in prep.)[6], which paper also describes our extension of the SO_2 rate coefficients by Green (1995) to higher energy levels. No rate coefficients are available for NS, so its excitation was assumed to be thermalized at the temperature of each grid point of the model. The population of the $^2\Pi_{3/2}$ state of NS, which lies 225 K above the $^2\Pi_{1/2}$ state, was assumed to be negligible. In the case of H_2S, Ball et al. (1999) measured the $1_{10} - 1_{01}$ rate coefficient in collisions with He at $T = 1.36 - 35.3$ K. Our model uses the rate coefficients by Green et al. (1993) for H_2O–He, multiplied by 2.6 based on comparison with the Ball et al. data, and scaled for the different reduced mass of the H_2S–H_2 system. Turner (1996) lists reasons why H_2S rate coefficients are likely to be larger than H_2O values.

4.2. Physical structure

The temperature and density structures of all our sources but MonR2 IRS3 were derived by van der Tak et al. (2000b). We have followed the same procedure to infer the structure of MonR2 IRS3, assuming a power-law density structure $n = n_0(r/r_0)^{-\alpha}$. The temperature profile is derived from the observed luminosity of 1.3×10^4 $L_\odot$ (Henning et al. 1992), while n_0 is constrained by the submillimeter photometry of Giannakopoulou et al. (1997). These dust models solve the grain heating and cooling self-consistenely, using opacity model 5 from

---

[5] http://talisker.as.arizona.edu/~michiel/ratran.html

[6] http://www.strw.leidenuniv.nl/~moldata

Ossenkopf & Henning (1994). These "OH5" opacities are the only ones that yield dust masses consistent with $C^{17}O$ measurements of AFGL 2591, where CO depletion is known to be negligible (van der Tak et al. 1999). To constrain α, the CS and $C^{34}S$ line spectrum of MonR2 IRS3 was modeled with the Monte Carlo program. Besides our own JCMT measurements (Table 5), data from Tafalla et al. (1997) and Choi et al. (2000) were used. The best fit was obtained for $\alpha = 1.25$ (Table 8), with a reduced $\chi^2 = 2.33$ over 11 degrees of freedom, although $\alpha = 1.0$ ($\chi^2 = 3.1$) and $\alpha = 1.5$ ($\chi^2 = 3.8$) also give acceptable fits. Radial profiles of 350 μm dust emission for our sources indicate larger values of α, by up to 0.5, than CS line emission (Mueller et al. 2002). If this difference holds more generally, it may reflect a reduced CS abundance at small radii, although the models of § 5.2 do not predict that.

Table 8. Power law model $n = n_0(r/r_0)^{-\alpha}$ for the density structure of MonR2 IRS3.

Parameter	Value
Outer radius r_0	0.3 pc
Inner radius	0.001 pc
α	1.25
n_0 (H_2)	1.21×10^4 cm^{-3}
CO/H_2	8×10^{-5}
Dust mass	1.05 $M_\odot$

4.3. Molecular abundances

Table 9 lists the results of the radiative transfer analysis, with the same source ordering as in Table 7. Abundances, if assumed constant, are $\sim 10^{-8}$ for OCS, $\sim 10^{-9}$ for H_2S, H_2CS, SO and SO_2, and $\sim 10^{-10}$ for HCS^+ and NS. These trends are the same as found above for beam-averaged column densities (§ 3.3); the Monte Carlo analysis does not change results by factors of more than a few. Except for SO, SO_2 and OCS, the source-to-source spread in the abundances is less than a factor of 10, and not related to temperature. These molecules (CS, H_2S, H_2CS, NS and HCS^+) appear to trace the chemically inactive outer envelope ($T < 100$ K), at least in the observed transitions. However, the high OCS abundances occur all in warm sources.

For SO and SO_2, the number of detected lines is large enough to investigate their abundances as a function of radius. Figure 4 shows that the Monte Carlo models fit the SO lines uniformly well over the observed range of energy levels for all sources except W 33 A: there is no indication for changes in the SO abundance between $T = 30$ and 90 K. In the case of W 33 A, some of the observed values appear to be higher than the models, which may be due to an uncertain high-velocity contribution for these lines. Observations of higher-excitation SO lines ($N = 10 \rightarrow 9$ near 430 GHz or $N = 11 \rightarrow 10$ near 473 GHz) would be valuable to investigate the effect of evaporating ice mantles on the abundance of SO.

Figure 5 shows the results of the models for SO_2. Models with $SO_2/H_2 \sim 10^{-9}$ fit the lines with $E_u \lesssim 100$ K within factors of a few. However, these models underproduce the lines with $E_u \gtrsim 100$ K by factors of $\gtrsim 100$. This discrepancy is best seen for W3 IRS5, W33A and AFGL 2591, where the most SO_2 lines are detected. For these sources, we have run models where the SO_2 abundance increases sharply ('jumps') when $T > 100$ K. These models are shown as triangles in Fig. 5 and quantified in Table 10. The SO_2 abundance increases by a factor of 100 in the case of W3 IRS5 and W33A, and by a factor of 1000 for AFGL 2591. These models reproduce all observed SO_2 lines to factors ~ 10. The residuals are considerably bigger than the expected error bars of factors of 2...3, mainly due to the uncertain high-velocity contribution, which suggests that more detailed modeling is needed. However, these 'jump' models fit the data much better than models where the SO_2 abundance is constant. The SO_2 abundances derived from the high-excitation lines are similar to those based on the infrared data, indicating that the same gas is probed. The data for the other sources are consistent with similar abundance jumps, but not enough high-excitation SO_2 lines have been detected to constrain such models. However, the data of AFGL 2136, NGC 7538 IRS1 and MonR2 IRS3 allow estimates of SO_2 abundances in their inner envelopes, which Table 10 also lists. Except NGC 6334 IRS1, the jumps in the SO_2 abundance occur all in sources with high $T(CH_3OH)$, confirming that the abundance enhancement is related to high temperatures, probably through ice evaporation.

Table 10. Models with SO_2 abundance 'jumps'.

Source	$(SO_2/H_2)_{\rm out}$ 10^{-9}	$(SO_2/H_2)_{\rm in}$ 10^{-7}
W3 IRS5	10	10
MonR2 IRS3	1	12[b]
AFGL 2136	0.5	0.8[b]
W33A	1	1
AFGL 2591	2	2
NGC 7538 IRS1	1	14[b]
IRAS 16293[a]	0.5	1

[a] From Schöier et al. (2002).
[b] Estimated value.

The models discussed so far assumed a static envelope and aimed to describe the low-velocity gas. To investigate whether the high-velocity gas could be due to infalling motions, we have modeled the SO emission from W3 IRS5 under the assumption of gravitational infall. In this model, the infall velocity $V_{\rm inf}$ varies with radius R as $\sqrt{GM/R}$, where G is the gravitational constant. The luminosity of

Table 9. Molecular abundances and abundance ratios: outer envelope

Source	SO 10^{-9}	SO_2 10^{-9}	OCS 10^{-9}	CS^a 10^{-9}	H_2S 10^{-9}	H_2CS 10^{-10}	NS 10^{-11}	HCS^+ 10^{-10}	SO/ SO_2	SO_2/ CS	SO/ CS	H_2S/ CS	NS/ CS
NGC 7538 IRS9	1	0.5	2	10	3	10	1	5	2	0.05	0.1	0.8	0.001
S140 IRS1	2	1	<2	5	2	7	1	5	2	0.2	0.4	0.8	0.002
W3 IRS5	10	10	0.5	5	3	3	...	0.2	1	2	2	2	...
MonR2 IRS3	5	1	...	5	<2	7	<1	...	5	0.2	1	<0.8	...
AFGL 2136	1	0.5	...	4	<1	3	<0.5	1	2	0.1	0.25	<0.5	<0.001
W33A	1	1	20	5	3	13	2	2	1	0.2	0.2	2	0.004
AFGL 2591	10	2	10	10	8	3	0.5	2	10	0.1	1	2	0.0005
NGC 7538 IRS1	5	1	2	10	3	10	1	2	5	0.1	0.5	0.8	0.001
NGC 6334 IRS1	2	2	50	10	0.4	7	10	2	1	0.2	0.2	1	0.01
Hot cores[b]	4	20	5	8	9	6	80	...	0.2	2	0.5	1	0.1
PDRs[c]	9	0.1	...	20	6	...	...	...	100	0.005	0.5	0.3	...
Dark clouds[d]	20	4	2	1	0.8	6	...	0.6	5	4	20	0.8	...
Shocks[e]	200	100	10	4	4000	8	...	0.1	2	25	50	1000	...
Low mass protostars[f]	4	0.6	7	3	2	4	...	0.2	10	0.2	1	0.7	...

[a] From van der Tak et al. (2000b), except MonR2 IRS3
[b] Source average from Hatchell et al. (1998b)
[c] Orion Bar: Jansen et al. (1995)
[d] L134N: Ohishi et al. (1992)
[e] Orion Plateau: Sutton et al. (1995); Minh et al. (1990)
[f] IRAS 16293-2422: Schöier et al. (2002)

W3 IRS5, if due to a single star, suggests a stellar mass of ≈30 $M_\odot$ (Vacca et al. 1996), so that $V_{\rm inf}$ ranges from 0.45 to 10.66 km s^{-1} in the model. However, the synthetic SO line profiles in 14–18″ beams have widths of 5–6 km s^{-1} FWHM, much less than the observed value of 13.5 km s^{-1}. Since the other sources have lower luminosities (hence infall speeds), it seems unlikely that the high-velocity SO and SO_2 emission is solely due to infall.

5. Discussion

5.1. Comparison to other objects

Tables 9 and 10 also list molecular abundances in other regions. Only the case of the low-mass protostar IRAS 16293 has been analyzed to the same level of detail as done here. To reduce uncertainties introduced by methodological differences, the table contains abundances scaled to the value of the commonly observed CS molecule. Using ratios also facilitates comparison with chemical models, because these are independent of the total amount of sulphur in the gas phase, which is not well-understood. Ultraviolet observations of diffuse clouds toward ζ Oph indicate that sulphur is undepleted from its solar abundance of $\sim 2\times10^{-5}$ (Savage & Sembach 1996). However, for dense clouds, it is unclear what fraction of sulphur is locked up in dust grains.

The ratios observed in our sources differ considerably from those in PDRs, dark clouds and shocks, indicating that in those regions, other chemical processes dominate. The ratios in IRAS 16293 are at the low end of the values found here, suggesting that in low-mass objects, depletion of molecules onto grains is more important.

In the case of hot cores, both abundance ratios and absolute abundances are similar to those observed here. The chemical similarity of our sources with hot cores prompts us to compare our results with chemical models invoking ice evaporation. Our assumption is that source-to-source differences in abundances are due to age differences, rather than to differences in initial physical or chemical conditions.

5.2. Comparison with chemical models

The sulphur chemistry of hot cores, where ice mantles are evaporating off dust grains and start a high-temperature chemistry, was studied by Charnley (1997). The model assumes that the dominant form of sulphur in the ices is H_2S, which after evaporation is destroyed by H and H_3O^+ to form S and H_3S^+. Reactions with OH and O_2 make first SO and then SO_2. Some H_2S reacts with C^+ into CS, which reacts with OH to make OCS. The sulphur chemistry strongly depends on temperature through its connection with the oxygen chemistry. At $T \gtrsim 300$ K, the SO_2 abundance remains factors of 10–100 below that of SO because O and OH are driven into H_2O. Results also depend on the presence of O_2 in the ice mantles. Observational limits on solid and gaseous O_2 (Vandenbussche et al. 1999; Goldsmith et al. 2000; Pagani et al. 2003) do not firmly rule out either assumption, but do make the model without O_2 ice more plausible. However, this model cannot directly be compared with our observations, which probe a mixture of warm and cold gas.

The chemistry of protostellar envelopes was modeled by Doty et al. (2002). In the inner warm region, a hot core chemistry similar to that of Charnley (1997) is used, whereas in the cold outer parts, a low-temperature chemistry including freeze-out is adopted. The initial conditions of the model depend on temperature to mimic the effect of ice evaporation. Although Doty et al. adopt the specific temperature and density structure of AFGL 2591 as modeled by van der Tak et al. (2000b), their results do not change by factors of more than a few for our other sources, which have temperature and density distributions similar to those of AFGL 2591.

The Doty et al. (2002) model has most gas-phase sulphur initially in S at $T < 100$ K ($S/H_2=6\times10^{-9}$) and in H_2S at $T > 100$ K ($H_2S/H_2=1.6\times10^{-6}$) to mimic the effect of ice evaporation. This choice of initial conditions is consistent with the nondetection of the [S I] line at 25.249 μm toward our sources with ISO. The upper limit of $\tau < 0.01$ in absorption implies $N(\mathrm{S}) < 5\times10^{15}$ cm^{-2}, so that for $N(H_2) \sim 10^{23}$ cm^{-2}, $S/H_2 < 5\times10^{-8}$, indicating that not all gas-phase sulphur in the inner envelope can be in atomic form. The inferred abundances imply that SO_2 is one of the dominant sulphur-bearing gas-phase molecules in the warm inner envelope. However, the sum of all sulphur-bearing molecules in the gas phase is still much lower than the value derived for diffuse clouds (Savage & Sembach 1996). Unless a major sulphur-bearing gas-phase species has been missed in this survey, $\sim$90% of the sulphur must be in a solid form which has not yet been detected.

Infrared observations of our sources with ISO-SWS do not support the assumption that H_2S is the main sulphur reservoir of the grain mantles. Toward W33A, a source with large ice abundances, the 3.98 μm band of solid H_2S is not detected to $\tau < 0.02$, which using a band strength of 5×10^{-18} cm mol^{-1} gives $N_s(H_2S) < 3.6\times10^{17}$ cm^{-2}, or $N_s(H_2S)/N_s(H_2O) < 0.03$ (W. Schutte, priv. comm.). However, solid OCS was detected with an abundance of $N_s(\mathrm{OCS})/N_s(H_2O) = (0.4-1)\times10^{-3}$ or $OCS/H_2 = (4-14)\times10^{-8}$ (Palumbo et al. 1997). Evaporation of solid OCS may explain our measured gas-phase OCS abundances which are otherwise unaccounted for. W 33 A is the only source in our sample for which both gas-phase and solid OCS have been detected. The results imply a gas/solid ratio of $\sim$0.5, much higher than that found for e.g. H_2O and CO_2 in this source (Boonman et al. 2003; Boonman & van Dishoeck 2003). Observations of both gas-phase and solid-state OCS toward other sources are needed to determine the role of grain-mantle evaporation. Observations of OCS lines from a wide range of energy levels may reveal an abundance increase at $T \gtrsim 100$ K, as indeed found for IRAS 16293 (Schöier et al. 2002). The low T_{ex} of H_2S and the high value of OCS (§ 3.2) support these conclusions.

The effect of evaporating OCS-rich ice mantles on hot core chemistry is explored by Doty et al. (2003). Briefly, the gas-phase abundances of CS, HCS^+ and OCS increase about linearly with the fraction of solid OCS, while those of H_2S, SO and SO_2 decrease about linearly. The H_2CS molecule is not affected much. Since the gas-phase chemistry of CS, HCS^+ and OCS depends only weakly on time, the use of sulphur molecules as chemical clock diminishes when H_2S is only a minor sulphur carrier in the ice mantles. However, the 'jump' models for SO_2 (Table 10) indicate that either H_2S or SO_2 is present in the grain mantles. The limits on solid SO_2 from infrared observations are not very stringent (Boogert et al. 1998).

We have compared our observations to the models of Doty et al. (2002), modified to have OCS in the evaporating ice mantles (S. Doty, priv. comm.). This model reproduces our observed abundances of CS, SO and H_2CS in the outer envelopes (Table 9) to within factors of a few for chemical ages of $\sim10^5$ yr. The abundances of SO_2 in the inner envelopes (Table 10) are also reproduced for the same chemical age. The model abundances of HCS^+ and SO_2 in the outer envelopes are factors of $\sim$10 below the observed values, which may be due to the adopted initial conditions, or the chemical network, which is based on the UMIST reaction rate database (Le Teuff et al. 2000)[7]. The outer envelope abundances of H_2S and OCS are underproduced even more (factors of $\sim$100). However, the small number of observed lines forced us to assume constant abundances for these species, while they may in fact be confined to the inner envelopes.

5.3. The role of shock chemistry

As an alternative to ice evaporation models, we consider the effect of non-dissociative shocks on the molecular envelopes surrounding the protostars. Such shocks occur by the interaction of the molecular outflows of protostars with their envelopes. Shocks fast enough to dissociate H_2 ($v \gtrsim 40$ km s^{-1}) would have a major impact on their molecular composition which our data do not indicate. Although our sources show outflows faster than that, both in infrared absorption (Mitchell et al. 1991) and in submillimeter emission (Mitchell & Hasegawa 1991; Mitchell et al. 1992) of CO, their filling factor must be small.

Our observed SO, SO_2 and H_2S abundances in the outer envelopes are consistent with those in postshock gas if sulphur was initially in molecular form (Leen & Graff 1988). The observed similarity of these abundances is not reproduced by the Pineau des Forêts et al. (1993) model which has most sulphur initially in atomic form. However, the two models are hard to compare because one is a two-fluid treatment, while the other treats neutral and charged particles as one fluid. Before concluding that postshock gas reproduces our data, we recommend that a two-fluid calculation is performed with most sulphur initially in molecular form.

Two other molecules suggest that the envelopes of young high-mass stars may have been processed by shocks, although neither one conclusively. First, ISO-SWS data show low ratios of gas-phase to solid-state CO_2 ($\lesssim 0.1$; van Dishoeck 1998) and the CO_2 gas phase abundance remains low through the 100–300 K temperature regime. After evaporating off grains, CO_2 must be promptly destroyed, which shocks can do in reactions with H (Charnley & Kaufman 2000) or perhaps H_2 (Doty et al. 2002; Talbi & Herbst 2002). Second, Hatchell & Viti (2002) measured NS/CS ratios of 0.02-0.05 in a sample of six hot cores and interpreted these as evidence for shocks. The main reactions to form NS require SH and NH which are produced from OH. Shocks use OH to form H_2O and suppress the production of NS. The values of NS/CS=0.001 – 0.01 measured here may indicate that shocks play a role too. However, for $t = 3 \times 10^4$ yr, the Doty et al. (2002) model also predicts NS/CS $\sim 10^{-3}$, so this ratio cannot be used to demonstrate the influence of shocks.

---

[7] http://www.rate99.co.uk

6. Conclusions

Submillimeter observations of SO, SO_2, H_2S, H_2CS, OCS, NS and HCS^+ toward nine embedded massive stars show that:

1. High-velocity gas contributes 10–50% to the CS, SO and SO_2 emission in $15 - 20''$ beams. This gas may either trace the outflows which are also seen in CO, or they may trace infall motions.
2. The SO_2 abundance increases from dark cloud levels in the outer envelope ($T < 100$ K) to levels seen in hot cores and shocks in the inner envelope ($T > 100$ K).
3. Molecular abundances are consistent with a model of ice evaporation in an envelope with gradients in temperature and density for a chemical age of $\sim 10^5$ yr.
4. The high observed abundance of OCS, the fact that $T_{\rm ex}({\rm OCS}) \gg T_{\rm ex}({\rm H_2S})$, and the detection of solid OCS and limit on solid H_2S all suggest that OCS is a major sulphur carrier in grain mantles, rather than H_2S.
5. For most other sulphur-bearing molecules, the source-to-source abundance variations by factors of up to 10 do not correlate with previously established evolutionary trends in temperature tracers. These species probe the chemically inactive outer envelope. Our data set does not constrain the abundances of H_2S and SO in the inner envelope, which, together with SO_2, are required to use sulphur as a clock.

These conclusions could be followed up by, respectively:

1. interferometric observations at $\lesssim 1''$ resolution of SO lines from a wide range of energy levels.
2. similar interferometric observations of SO_2.
3. updating the model of Leen & Graff (1988) using a two-fluid treatment, and extending it to later times.
4. a multi-line study of OCS, covering energy levels well above and well below 100 K.
5. observations of high-excitation SO and H_2S lines, e.g. SO 430 and 473 GHz and H_2S 369 GHz.

Items 3 and 4 are within the capabilities of current computational and observational facilities. The CSO and JCMT may be able to carry out item 5 in very good weather, but the future Atacama Pathfinder Experiment (APEX) can benefit from an even better site. Current interferometers are not sensitive enough for items 1 and 2, which require observing several lines and several sources. However, future instruments such as the Combined Array for Research into Millimeter Astronomy (CARMA) and the Atacama Large Millimeter Array (ALMA) will be well-suited for these projects.

Acknowledgements. The authors thank the JCMT and IRAM staffs for their support, Malcolm Walmsley, Holger Müller, Jennifer Hatchell and Xander Tielens for useful discussions, and Willem Schutte, Fred Lahuis and Steve Doty for input. Astrochemistry in Leiden is supported by the Nederlandse Organisatie voor Wetenschappelijk Onderzoek (NWO) through grant 614-41-003 and a Spinoza award.

References

Ball, C. D., Mengel, M., De Lucia, F. C., & Woon, D. E. 1999, J. Chem. Phys., 111, 8893
Beers, Y., Klein, X., Kirchhoff, W. H., & Johnson, D. R. 1972, J. Mol. Sp., 44, 553
Blake, G. A., Sutton, E. C., Masson, C. R., & Phillips, T. G. 1987, ApJ, 315, 621
Boogert, A. C. A., Ehrenfreund, P., Gerakines, P. A., et al. 2000, A&A, 353, 349
Boogert, A. C. A., Helmich, F. P., van Dishoeck, E. F., et al. 1998, A&A, 336, 352
Boonman, A. M. S. & van Dishoeck, E. F. 2003, A&A, 403, 1003
Boonman, A. M. S., van Dishoeck, E. F., Lahuis, F., & Doty, S. D. 2003, A&A, 399, 1063
Boonman, A. M. S., Wright, C. M., & van Dishoeck, E. F. 1999, in 3rd Cologne-Zermatt Symposium, Eds.: V. Ossenkopf, J. Stutzki, and G. Winnewisser, 275
Buckle, J. V. & Fuller, G. A. 2003, A&A, 399, 567
Charnley, S. B. 1997, ApJ, 481, 396
Charnley, S. B. & Kaufman, M. J. 2000, ApJ, 529, L111
Choi, M. 2002, ApJ, 575, 900
Choi, M., Evans, N. J., Tafalla, M., & Bachiller, R. 2000, ApJ, 538, 738
Doty, S. D., Schöier, F. L., & van Dishoeck, E. F. 2003, A&A, submitted
Doty, S. D., van Dishoeck, E. F., van der Tak, F. F. S., & Boonman, A. M. S. 2002, A&A, 389, 446
Giannakopoulou, J., Mitchell, G. F., Hasegawa, T. I., Matthews, H. E., & Maillard, J. 1997, ApJ, 487, 346
Goldsmith, P. F., Melnick, G. J., Bergin, E. A., et al. 2000, ApJ, 539, L123
Green, S. 1995, ApJS, 100, 213
Green, S., Maluendes, S., & McLean, A. D. 1993, ApJS, 85, 181
Hatchell, J., Thompson, M. A., Millar, T. J., & MacDonald, G. H. 1998a, A&AS, 133, 29
—. 1998b, A&A, 338, 713
Hatchell, J. & Viti, S. 2002, A&A, 381, L33

Helmich, F. P., Jansen, D. J., de Graauw, T., Groesbeck, T. D., & van Dishoeck, E. F. 1994, A&A, 283, 626

Helmich, F. P. & van Dishoeck, E. F. 1997, A&AS, 124, 205

Henning, T., Chini, R., & Pfau, W. 1992, A&A, 263, 285

Hogerheijde, M. R. & van der Tak, F. F. S. 2000, A&A, 362, 697

Jansen, D. J., Spaans, M., Hogerheijde, M. R., & van Dishoeck, E. F. 1995, A&A, 303, 541

Keane, J. V., Boonman, A. M. S., Tielens, A. G. G. M., & van Dishoeck, E. F. 2001, A&A, 376, L5

Langer, W. D., van Dishoeck, E. F., Bergin, E. A., et al. 2000, Protostars and Planets IV, 29

Le Teuff, Y. H., Millar, T. J., & Markwick, A. J. 2000, A&AS, 146, 157

Lee, C., Mundy, L. G., Stone, J. M., & Ostriker, E. C. 2002, ApJ, 576, 294

Leen, T. M. & Graff, M. M. 1988, ApJ, 325, 411

McCutcheon, W. H., Sandell, G., Matthews, H. E., et al. 2000, MNRAS, 316, 152

Minh, Y. C., Irvine, W. M., McGonagle, D., & Ziurys, L. M. 1990, ApJ, 360, 136

Mitchell, G. F. 1984, ApJ, 287, 665

Mitchell, G. F. & Hasegawa, T. I. 1991, ApJ, 371, L33

Mitchell, G. F., Hasegawa, T. I., & Schella, J. 1992, ApJ, 386, 604

Mitchell, G. F., Maillard, J.-P., & Hasegawa, T. I. 1991, ApJ, 371, 342

Mueller, K. E., Shirley, Y. L., Evans, N. J., & Jacobson, H. R. 2002, ApJS, 143, 469

Nummelin, A., Bergman, P., Hjalmarson, Å., et al. 2000, ApJS, 128, 213

Ohishi, M., Irvine, W. M., & Kaifu, N. 1992, in IAU Symp. 150: Astrochemistry of Cosmic Phenomena, 171

Ossenkopf, V. & Henning, T. 1994, A&A, 291, 943

Pagani, L., Olofsson, A. O. H., Bergman, P., et al. 2003, A&A, 402, L77

Palumbo, M. E., Geballe, T. R., & Tielens, A. G. G. M. 1997, ApJ, 479, 839

Pickett, H. M., Poynter, R. L., Cohen, E. A., et al. 1998, J. Quant. Spectrosc. Radiat. Transfer, 60, 883

Pineau des Forêts, G., Roueff, E., Schilke, P., & Flower, D. R. 1993, MNRAS, 262, 915

Savage, B. D. & Sembach, K. R. 1996, ARA&A, 34, 279

Schilke, P., Groesbeck, T. D., Blake, G. A., & Phillips, T. G. 1997, ApJS, 108, 301

Schöier, F. L., Jørgensen, J. K., van Dishoeck, E. F., & Blake, G. A. 2002, A&A, 390, 1001

Sutton, E. C., Peng, R., Danchi, W. C., et al. 1995, ApJS, 97, 455

Tafalla, M., Bachiller, R., Wright, M. C. H., & Welch, W. J. 1997, ApJ, 474, 329

Talbi, D. & Herbst, E. 2002, A&A, 386, 1139

Turner, B. E. 1996, ApJ, 468, 694

Vacca, W. D., Garmany, C. D., & Shull, J. M. 1996, ApJ, 460, 914

van der Tak, F. F. S., van Dishoeck, E. F., & Caselli, P. 2000a, A&A, 361, 327

van der Tak, F. F. S., van Dishoeck, E. F., Evans, N. J., Bakker, E. J., & Blake, G. A. 1999, ApJ, 522, 991

van der Tak, F. F. S., van Dishoeck, E. F., Evans, N. J., & Blake, G. A. 2000b, ApJ, 537, 283

van Dishoeck, E. F. 1998, Faraday Discussion, 109, 31

—. 2001, The Promise of the Herschel Space Observatory. Eds. G.L. Pilbratt, J. Cernicharo, A.M. Heras, T. Prusti, & R. Harris. ESA-SP, 460, 185

Vandenbussche, B., Ehrenfreund, P., Boogert, A. C. A., et al. 1999, A&A, 346, L57

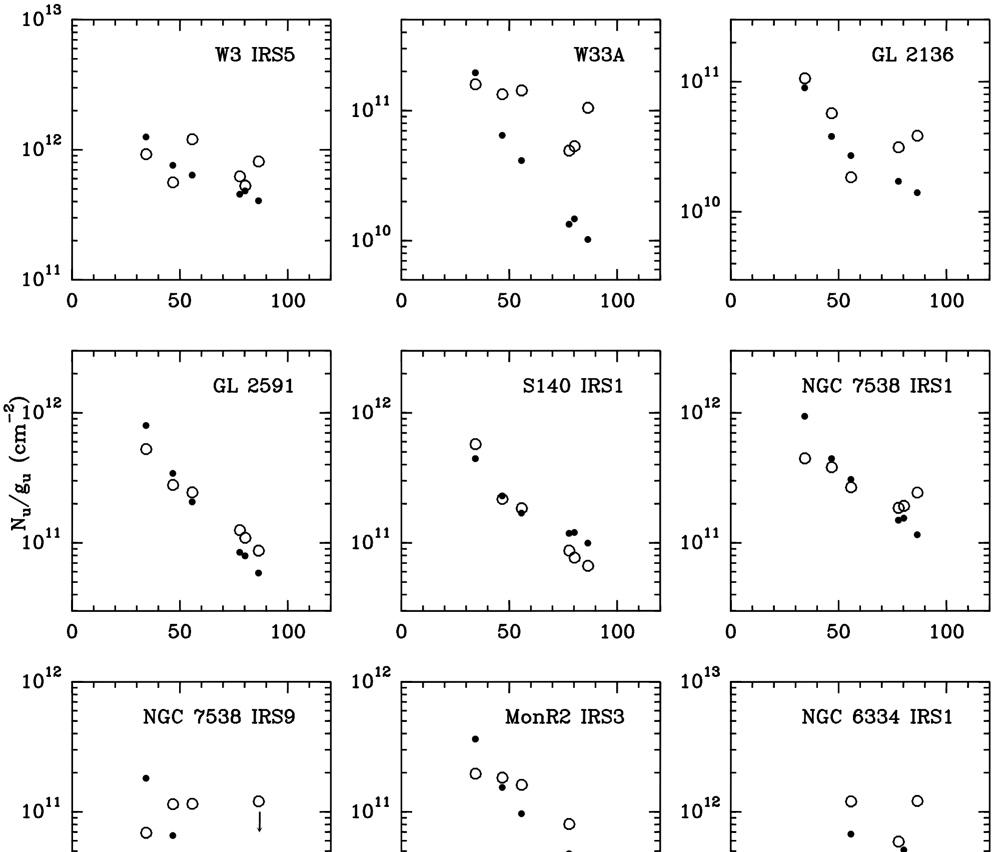

Fig. 4. Observatio of SO (open circles; envelope component only), and predictions from Monte Carlo models (filled dots). Line fluxes have been converted to upper state column densities following Helmich et al. (1994). The estimated error on the line fluxes is a factor of two, due to the uncertain contri-

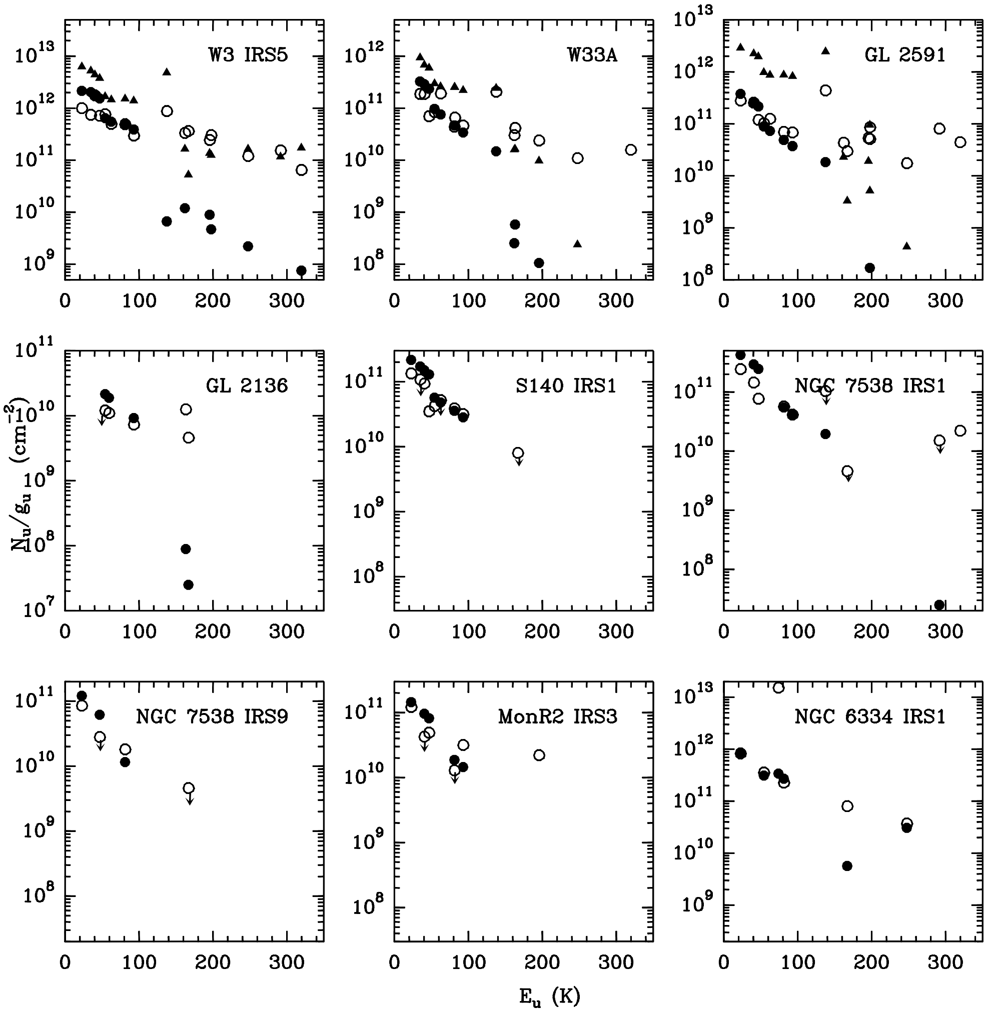

Fig. 5. As previous figure, for SO$_2$. Triangles indicate models with a temperature-dependent SO$_2$ abundance.